

Analysis of Charge Carrier Transport Toward Optimized Cathode Composites for All-Solid-State Li–S Batteries

Georg F. Dewald,^[a, b] Saneyuki Ohno,^[a, b, c] Joachim G. C. Hering,^[a, b] Jürgen Janek,^{*[a, b]} and Wolfgang G. Zeier^{*[d]}

A high theoretical energy density makes lithium-sulfur (Li–S) batteries promising candidates for energy storage systems of the post-lithium-ion generation. As the performance of Li–S cells with liquid electrolytes is impaired by the solubility of reaction intermediates, solid-state cell concepts represent an auspicious approach for future electrochemical energy storage. However, the kinetics of Li–S solid-state batteries and high charge/discharge rate still remain major challenges, and in-depth knowledge of the charge carrier transport in solid-state composite sulfur cathodes is still missing. In this work, the

charge transport and cyclability of composite cathodes consisting of sulfur, $\text{Li}_6\text{PS}_5\text{Cl}$ and carbon, with varying volume fractions of ion- and electron-conducting phases is investigated. The limiting thresholds of charge transport are elucidated by comparing the battery performance with effective transport properties of the cathode composite. Although both the effective electronic and ionic conductivities indicate high tortuosity factors, ionic transport is identified as a critical bottleneck. This work underscores the importance of quantitative transport analysis as a tool for cathode optimization.

1. Introduction

Lithium-sulfur (Li–S) batteries are often considered as a promising advancement of conventional lithium-ion batteries (LIBs), as the conversion-type cell reaction leads to high theoretical specific energies.^[1–6] While detrimental side reactions and transport mechanisms such as the dissolution of reaction intermediates (polysulfide shuttle)^[7–12] are impairing Li–S batteries with liquid electrolytes, progress in the field of solid electrolytes (SEs) is drawing attention to all-solid-state cell concepts.^[13–19] Here, a solid separator made from a single-ion

conducting SE physically suppresses the polysulfide shuttle. Developments of highly conductive SEs are contributing to the remarkable progress in this field over the past years.^[20–24] Among the various lithium SEs, lithium thiophosphates stand out due to high ionic conductivity and room-temperature processability.^[25–29] While these materials suffer from degradation due to their relatively poor chemical stability,^[30–34] the low redox potential of the sulfur cathode aligns with the low oxidative stability of these electrolytes and – in principle – stable long-term operation should be possible.

In the case of Li–S batteries with liquid electrolytes, a strong influence of cathode design, e.g. regarding electrolyte content and structured carbon scaffolds, on the cycling performance was reported, underscoring the potential of electrode “architecture” optimization.^[35–42] However, the insulating character of the active material sulfur, as well as its significant volume change during cell cycling, lead to specific design challenges for all-solid-state Li–S cells.^[43,44] To fully exploit the theoretical capacity, the cathode “architecture” and microstructure need to provide well percolating electronic and ionic conduction pathways with sufficient effective partial conductivities. Therefore, the implementation of conductive additives, typically carbon, is a necessity to ensure sufficient effective electronic conductivity. However, as the addition of carbon has been reported to support the decomposition of thiophosphate electrolytes,^[45–48] a carefully balanced implementation of the conductive additive is required for long-term stable batteries. As the impact of reactions at the SE-carbon interface depends on the interfacial area between the components, the electrochemical degradation is affected by the microstructure of cathode composites. Furthermore, chemomechanical failure, e.g. the loss of contact during cycling, represents another critical degradation mechanism in solid-state batteries (SSBs), and it seems particularly prominent in

- [a] G. F. Dewald, Prof. S. Ohno, J. G. C. Hering, Prof. J. Janek
Institute of Physical Chemistry
Justus-Liebig-University Giessen
Heinrich-Buff-Ring 17, 35392 Giessen, Germany
E-mail: Juergen.Janek@phys.chemie.uni-giessen.de
- [b] G. F. Dewald, Prof. S. Ohno, J. G. C. Hering, Prof. J. Janek
Center for Materials Research (LaMa)
Justus-Liebig-University Giessen
Heinrich-Buff-Ring 16, 35392 Giessen, Germany
- [c] Prof. S. Ohno
Department of Applied Chemistry, Graduate School of Engineering
Kyushu University
744 Motooka, Nishi-ku, 819-0395 Fukuoka, Japan
- [d] Prof. W. G. Zeier
Institute of Inorganic and Analytical Chemistry
University of Münster
Correnstrasse 30, 48149 Münster, Germany
E-mail: wzeier@uni-muenster.de

 Supporting information for this article is available on the WWW under
<https://doi.org/10.1002/batt.202000194>

 An invited contribution to a joint Special Collection between
ChemElectroChem and Batteries & Supercaps dedicated to research Beyond
Lithium-Ion Batteries

 © 2020 The Authors. Published by Wiley-VCH GmbH. This is an open access
article under the terms of the Creative Commons Attribution License, which
permits use, distribution and reproduction in any medium, provided the
original work is properly cited.

sulfur-based cathodes as the cell reaction is coupled with drastic volume changes of about 80%.^[8,43,49–52] Consequently, an optimized cathode microstructure, allowing for persistent contact between the components, is mandatory in sulfur-based all-solid-state cathodes to exploit the high theoretical performance. Following this approach, the positive effect of intense mixing processes, *e.g.* ball-milling, liquid-phase or gas-phase mixing, on the cycling performance of solid-state sulfur-based cathodes has been shown in the past,^[53–60] highlighting the potential of the solid-state Li–S cell concepts.

Despite the progress in recent years, a deeper understanding of the charge transport within the composite cathode is needed to pave the way for further optimization of all-solid-state Li–S batteries. Competitive SSBs require high areal loadings of active materials, exceeding those of typical lab-scale studies. Hence, the volume fractions of inactive battery components, *i.e.* electrolyte, current collectors, and conductive additives, need to be reduced – as it was already well achieved in LIBs.^[61–66] Kato *et al.* elucidated the performance of thick electrode configurations in graphite-LiCoO₂ solid-state cells, reporting the tortuous ion transport within the cathode to be limiting at a high areal capacity of about 15.7 mAh·cm⁻².^[67] For oxide cathode active materials, the influence of the microstructure on cell performance has been discussed in depth.^[68–75] The analysis of the effective transport properties of battery separators and electrodes clearly led to a deeper understanding of the underlying bottlenecks. Electrochemical and microscopic techniques, in combination with modeling of cathode composites, are established methods to characterize the influence of both ionic and electronic transport properties on the cell performance.^[76–86] For example, the particle size of the active materials has been shown to impact the overall cell performance significantly, paving the way for optimization strategies.^[68,70,72]

In the case of all-solid-state Li–S cells, detailed studies and quantitative analysis of the effective transport properties in cathode composites were rarely reported. The complex microstructure of solid-state sulfur-based cathode composites – which are at least three-phase systems – and the underlying bottlenecks for transport are challenging to assess spectroscopically and microscopically due to small particle sizes, low phase contrast of the materials and electron beam-sensitivity of the SE. While X-ray diffraction and X-ray photoelectron spectroscopy are widely used techniques to characterize aging and degradation of sulfur-based cathodes,^[43,87–89] any microstructural information is limited. For this reason, the electrochemical assessment of effective transport properties represents an essential tool to elucidate the ionic and electronic transport within solid-state cathode composites.^[67,71,90,91]

In order to exploit the potential of Li–S cells, in-depth studies on the influence of the composite microstructure of solid-state cathodes on the battery performance are needed. This work aims to shed light on the charge transport in solid-state sulfur cathodes by determining the effective transport properties of sulfur-thiophosphate-carbon cathode composites. By systematically altering volume fractions of SE and carbon, *i.e.* the ion- and electron-conducting phases, respectively, we

quantify the impact on the transport within these 3D disordered composites and analyze the effective transport properties as a function of the tortuosity factor and the corresponding volume fraction. By relating the effective conductivities of sulfur-based cathodes with their cycling performance, we identify the rate-limiting transport process, which is ionic transport. We find that while low volume fractions of carbon black are sufficient to ensure electronic percolation, high SE fractions are needed to access the theoretical capacity of sulfur. We even find that the processing of SE in the cathode composites lowers the ionic conductivity of the employed crystalline thiophosphate, highlighting the importance of further research on the influence of SE and cathode processing. This work shows that the implementation of low-tortuosity electrode architectures and/or highly conductive SEs is needed to increase the effective conductivities, in order to successfully implement thick electrode configurations for high-energy Li–S cells.

Experimental Section

Synthesis of solid electrolytes

All samples were handled under argon atmosphere ($p(O_2)/p < 1 \text{ ppm}$, $p(H_2O)/p < 5 \text{ ppm}$). The solid electrolyte Li₆PS₅Cl (SE) was synthesized in a 3 g batch via solid-state reaction using lithium sulfide (Li₂S, Sigma Aldrich, 99.98%), phosphorus pentasulfide (P₂S₅, Sigma Aldrich, 99%) and anhydrous lithium chloride (LiCl, Alfa Aesar, 99%) as reactants.

For the synthesis of Li₆PS₅Cl, the starting materials were mixed in stoichiometric ratios and ground for 15 min in an agate mortar. The mixture was pelletized and sealed under vacuum into an ampoule, followed by annealing at 823 K for 7 days (ramp 100 K·h⁻¹). After completion, the samples were manually ground.

The purity of Li₆PS₅Cl was checked with X-ray diffraction. Employing a PANalytical Empyrean powder diffractometer in Bragg-Brentano θ - θ geometry with Cu K α radiation ($\lambda_1 = 154.056 \text{ pm}$, $\lambda_2 = 154.539 \text{ pm}$), a 2 θ range of 15° to 90° was examined (step size: 0.026°, counting time per step 200 s). To protect the samples from the ambient atmosphere, a (911)-oriented Si zero background holder and a Kapton® polyimide film were used. The results can be found in the Supporting Information.

Electrical characterization

Ionic conductivity of the as-synthesized SE was probed via electrochemical impedance spectroscopy. Samples were prepared by densifying 100 mg of SE in a 10 mm diameter PEEK casing by 360 MPa for 3 min. With stainless steel rods as contacts, the measurement was performed in a frequency range from 7 MHz to 10 mHz with an excitation amplitude of 10 mV. The impedance data of the synthesized SE is shown in the Supporting Information.

Preparation of cathode composites

Elemental sulfur (Carl Roth, 99.5%) as well as carbon black (ECP600 JD, LION), were mixed in different ratios inside a planetary mixer (PMH 10, Netzsch Feinmahltechnik) with a rotation speed of 2000 rpm for 30 min under ambient atmosphere as previously described.^[43] After drying at 80 °C under a dynamic vacuum for

24 h, samples were transferred to an Ar-filled glovebox. Cathode composites were obtained by ball-milling S—C—Li₆PS₅Cl mixtures in 300 mg batches in a Fritsch Pulverisette 7 premium line (ZrO₂ milling set, 80 mL cups, 30 g of 5 mm diameter milling media) for 24 milling cycles of each 10 min at 500 rpm and a cooling break of 10 min. All cathode components employed in this study possess similar densities (sulfur: 2.09 g·cm⁻³, Li₆PS₅Cl: 1.85 g·cm⁻³, carbon black: approx. 2.0 g·cm⁻³).

Solid-state battery assembly

For cell testing, In/InLi|SE|S—C—SE stacks were assembled inside a custom-made PEEK casing. As the employed SE is not stable in contact with lithium metal,^[92] an In/InLi alloy anode was employed to avoid side reactions at the anode. To ensure reproducibility within this work, the fractions of electronically and ionically conducting phases within the solid-state cathode were varied, keeping the active material loading constant at 3.8 mg·cm⁻². For cell assembly, 80 mg of electrolyte and 10 mg of cathode composite were layered inside the cell casing and compressed uniaxially for 3 min under 380 MPa. Subsequently, a stack of 9 mm diameter indium foil (100 µm thickness, chemPur, 99.995%) and 6 mm diameter lithium foil (120 µm, Sigma-Aldrich, 99.9%) was placed on the separator. Due to fast solid-state diffusion at room temperature, the formation of an InLi alloy occurs.^[93] As current collectors, two stainless steel rods were employed. A pressure of approximately 60 MPa was applied before cycling to ensure sufficient contact between the components.

DC polarization experiments

Ion-blocking and electron-blocking cells for DC polarization experiments of cathode composites were assembled using 30 mg and 15 mg of composite, respectively. As ion-blocking electrodes, simple stainless-steel rods were employed for contacting. A stack of In/InLi|Li₆PS₅Cl|S—C—SE|Li₆PS₅Cl|In/InLi was used to probe the cathode composites under electron-blocking conditions. The argyrodite Li₆PS₅Cl was employed as an electron-blocking electrode as interfacial stability towards the In/InLi anode can be expected.^[94–96] For the densification of powdery components, the same parameters as described above were used. Due to the high pressure, a good contact of the electrode towards the cathode composite is assumed. The effective conductivities of the cathode composites were evaluated by DC polarization. For electronic conduction, constant potentials of 5 mV, -10 mV, 20 mV and -30 mV were applied for 6 h each with ion-blocking electrodes. Under electron-blocking conditions, constant potentials of 50 mV and -50 mV (12 h equilibration) were employed. Assuming the equilibrium current can be attributed to solely electronic or ionic transport under ion-blocking and electron-blocking conditions, respectively, the resistances are obtained from linear fitting of the I-U plot based on Ohm's law. By taking the sample geometry into account, the respective effective conductivities are obtained.

Electrochemical testing

All electrochemical experiments were performed at 298 K using a VMP300 potentiostat (Biologic). Li—S cells were cycled under galvanostatic conditions in a potential window of 1.0 V–2.4 V vs. In/InLi. C-rates were calculated based on the theoretical capacity of sulfur (1672 mAh·g_S⁻¹), assuming complete reduction to Li₂S. Long-term cycling stability was probed at a C-rate of 0.1 C (640 µA·cm⁻²).

2. Results

2.1. Cycling Results

In order to understand the influence of the volume fractions of non-active components on the cycling performance of solid-state sulfur cathodes, we first vary the ratio of lithium ion- and electron-conducting phases within the cathode, namely the SE and carbon fractions. For a realistic assessment towards commercialization, the loading of active material sulfur is kept constant in all cathode composites at a theoretical areal capacity of 6.4 mAh·cm⁻² (3.8 mg·cm⁻²) to provide a comparison of the resulting cell performances. The employed materials, Li₆PS₅Cl as well as the commercial carbon black, are frequently used in SSBs.^[43,45,54,96–99] While many publications focus on weight fractions when reporting the cathode contents as they matter for the specific energy, volume fractions are a more relevant metric to consider the impact of conducting phases as charge transport in disordered media directly scales with the fraction of the volume of the conducting phases, ϕ . The SE and carbon volume fractions within the total cathode composite, $\phi(\text{SE})$ and $\phi(\text{C})$, employed in this study are summarized in Figure 1a. Generally, high SE to C volume ratios ($\phi(\text{SE}) \cdot \phi(\text{C})^{-1}$), *i.e.* small carbon fractions, are expected to balance the effective ionic and electronic conductivities in view of the superior electronic conductivity of carbon black compared to the ionic conductivity of Li₆PS₅Cl.^[100–103] Hence, a nominal carbon volume fraction of 0.048 is chosen as the highest SE to C volume ratio in this study (corresponding to a ratio of the volume fractions of SE and carbon of $\phi(\text{SE}) \cdot \phi(\text{C})^{-1} = 14$). While keeping the nominal sulfur volume fraction constant at $\phi(\text{S}) = 0.29$, the $\phi(\text{SE}) \cdot \phi(\text{C})^{-1}$ ratio is varied (a full list of compositions can be found in Table S1). Although the volume fractions of 'inactive' electrode components, *i.e.* both SE and carbon fractions, need to be reduced for high-energy Li—S cells, the sulfur fraction is kept constant in this study to fix the current density for cycling and allow for a proper comparison. In this study, all cells are cycled in a potential window of 1.0–2.4 V vs. In/InLi with a current density of 640 µA·cm⁻² (0.1 C).^[104] It is important to note that Li—S cells are discharged in the initial step, *i.e.* sulfur is reduced to form Li₂S. The subsequent first charge-discharge cycle is referred to as the first cycle in the following.

The potential profiles of the first charge-discharge cycle are shown in Figure 1b for all characterized cathode compositions. For the sample with the lowest carbon volume fraction ($\phi(\text{SE}) \cdot \phi(\text{C})^{-1} = 14$), a capacity of only 235 mAh·g_S⁻¹ is achieved in the first discharge, despite the high theoretical capacity of sulfur (1672 mAh·g_S⁻¹). In contrast, cathodes with $\phi(\text{SE}) \cdot \phi(\text{C})^{-1} = 6.5$ and 4.0 almost achieve full sulfur utilization. In the cell with a higher carbon fraction in the composite ($\phi(\text{SE}) \cdot \phi(\text{C})^{-1} = 1.4$), again, lower capacities are observed. Here, a sloped discharge curve indicates a large overpotential and possible ionic transport limitations. Based on these results, there is an optimum range for $\phi(\text{SE}) \cdot \phi(\text{C})^{-1}$ for a given sulfur fraction, which in this study is between 6.5 and 2.7.

Results of prolonged cycling over 30 cycles further highlight the influence of the $\phi(\text{SE}) \cdot \phi(\text{C})^{-1}$ volume ratio within the cathode composite on cell performance (Figure 2a). A bar plot of selected

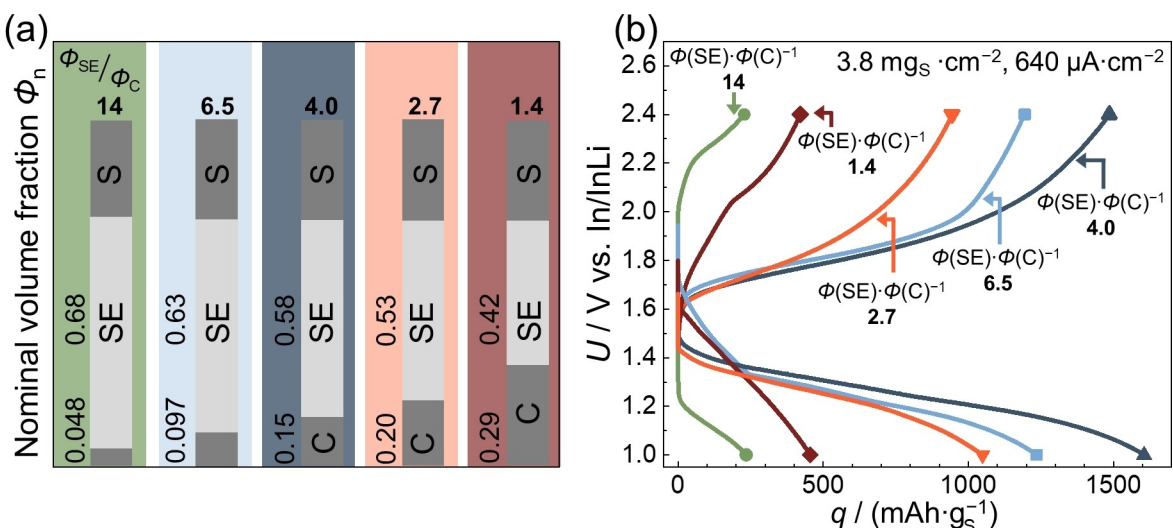


Figure 1. a) By varying the nominal volume fractions ϕ_n of electrolyte and carbon in sulfur-based cathode composites, thus the SE to C volume ratio ($\phi(\text{SE}) \cdot \phi(\text{C})^{-1}$), the influence of inactive cathode components on cell performance is studied. b) Charge-discharge curves obtained for the first cycle of In/InLi|Li₆PS₅Cl|S-C-Li₆PS₅Cl solid-state batteries highlight the influence of the SE and carbon volume fractions within the composite cathode on the sulfur utilization. While for the lowest carbon volume fraction only a small discharge capacity of 235 mAh·g_S⁻¹ is observed, $\phi(\text{SE}) \cdot \phi(\text{C})^{-1}$ of 4.0 and 6.5 allow for higher sulfur utilization. However, at smaller $\phi(\text{SE}) \cdot \phi(\text{C})^{-1}$, lower capacities indicate limitations in ionic transport at low SE fractions.

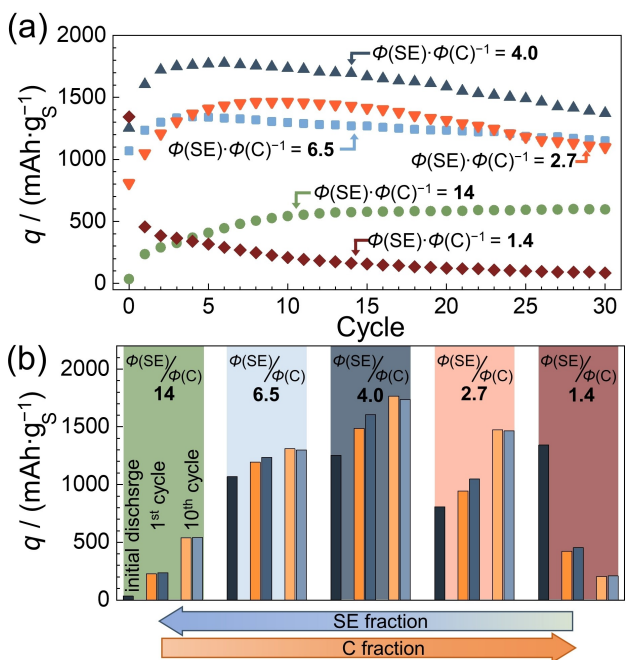


Figure 2. a) Cycling data for In/InLi|Li₆PS₅Cl|S-C-Li₆PS₅Cl SSB cells with various SE to carbon volume ratios ($\phi(\text{SE}) \cdot \phi(\text{C})^{-1}$) in the composite cathode. b) Bar plot of the obtained capacities during the initial discharge in comparison to the charge (orange) and discharge (blue) capacities for the first and 10th cycle helps for visualization of characteristics in long-term behaviors. A gradual increase of early capacities of the cathode with $\phi(\text{SE}) \cdot \phi(\text{C})^{-1} = 14$ ($\phi_n(\text{C}) = 0.048$) results in a stable capacity of around 500 mAh·g_S⁻¹ after 10 cycles, possibly caused by redox-active decomposition products of Li₆PS₅Cl.^[46,87,106] For $\phi(\text{SE}) \cdot \phi(\text{C})^{-1}$ of 2.7, 4.0 and 6.5, a comparable activation-type increase in capacities is found in the first cycles. Here, high capacities > 1000 mAh·g_S⁻¹ are still obtained over 30 cycles. Despite a high initial discharge capacity, the cathode with a high carbon fraction of 0.29 shows a pronounced degradation over prolonged cycling. For $\phi(\text{SE}) \cdot \phi(\text{C})^{-1}$ of 2.7, 4.0 and 6.5, high capacities > 1000 mAh·g_S⁻¹ are obtained over 30 cycles.

capacities further helps to visualize the differences in cycling performance over the first 10 cycles (Figure 2b). Potential profiles obtained for initial discharge are shown in the Supporting Information (Figure S1). Overall, samples with $\phi(\text{SE}) \cdot \phi(\text{C})^{-1}$ between 2.7 and 6.5 show the highest capacities during prolonged cycling up to 30 cycles. Despite a high initial discharge capacity of 1300 mAh·g_S⁻¹, a significant capacity fade is observed for the cathode with the smallest $\phi(\text{SE}) \cdot \phi(\text{C})^{-1}$ of 1.4.

While a minor capacity of 34 mAh·g_S⁻¹ is obtained for the initial discharge of the cathode with the lowest carbon fraction, steadily increasing discharge capacities are found for this sample over ongoing cycling, stabilizing at 500 mAh·g_S⁻¹ after 10 cycles. The increasing trend in the capacity in the early cycles is also observed for cathodes with higher carbon fractions. This behavior is often referred to as an *activation regime* and is proposed to indicate electrolyte degradation.^[43,105] In line with recent publications on the capacity contribution of thiophosphate electrolytes to the overall cell capacity,^[46,106,107] we attribute this mainly to the reversible cycling of SE decomposition products. The capacity of 500 mAh·g_S⁻¹ corresponds to a capacity of around 230 mAh·g_{SE}⁻¹ when it is normalized to the SE fraction of the respective cathode, which is well in line with recent publications on Li₆PS₅Cl-C cathodes.^[46,106] It is important to note, that the capacity contribution of the decomposition products will depend on the SE-C interfacial area, *i.e.* the $\phi(\text{SE}) \cdot \phi(\text{C})^{-1}$ volume ratio as well as particle sizes of the components. Coulombic efficiencies over 100% in the first cycles found for all cells further support the assumptions that the SE decomposes partly and that the thereby formed species can be cycled reversibly (Supporting Information, Figure S2a). The extent and slope of the activation-type increase in capacity appear to depend on the $\phi(\text{SE}) \cdot \phi(\text{C})^{-1}$ volume ratio. Considering the high surface area of the employed carbon black as well as the intense mixing via ball-milling, the decomposition of thiophosphate at the SE-C interface, followed by the reversible

cycling of decomposition products, is a conceivable mechanism here.^[32,48,87,106]

The drastic capacity fade observed for a $\phi(\text{SE}) \cdot \phi(\text{C})^{-1}$ of 1.4 after a high initial discharge capacity of 1340 mAh·g⁻¹ may be explained by the high SE–C interfacial area in this sample, possibly leading to massive electrolyte degradation, which may hinder ion transport in the composite.^[46] Additional degradation processes such as contact losses within the cathode during the volume contraction of active material during charging may also be contributing here.^[43] Cell deterioration is also highlighted by steadily increasing overpotentials during cycling (Supporting Information, Figure S2b). Full potential profiles for all cells can be found in the Supporting Information (Figures S3–S7). In the light of these results, a balanced implementation of ionically and electronically conducting phases into composite cathodes is required for stable, high-capacity cell performance. Within this study, the optimal range of $\phi(\text{SE}) \cdot \phi(\text{C})^{-1}$ appears to be 6.5–2.7 for the given sulfur volume fraction.

As a high fraction of the non-active material limits the achievable energy density of the resulting cell, a high sulfur loading, as well as low SE and carbon fractions are desired towards competitive all-solid-state Li–S batteries.^[5,108] However, too low volume fractions of the conducting phases in the composite cathodes clearly have a detrimental impact on the cycling performance based on the here-observed results. While a small volume fraction of carbon is enough to provide sufficient electron conduction, a larger volume fraction of the SE is required for better cyclability, resulting in the requirement of $\phi(\text{SE}) \cdot \phi(\text{C})^{-1}$ to be much higher than unity. It is also notable that the necessary carbon fraction is much larger than what is typically utilized in transition metal oxide-based cathodes in SSBs. Due to the electronic conductivity of the transition metal oxides, carbon is not mandatory to obtain a functional electrode here. If carbon is employed, typically a small amount (often < 5 wt.%, approx. corresponding to $\phi(\text{SE}) \cdot \phi(\text{C})^{-1} > 5$) is implemented.^[45,61,109–111] Overall, toward the rational design of the cathode composites, it is paramount to investigate the transport in the composite and, particularly for solid-state Li–S batteries, the effective conductivities in the ball-milled composites need to be investigated quantitatively.

2.2. Determination of Effective Transport Properties

For a quantitative discussion of charge carrier transport in composite cathodes, the effective ionic/electronic (partial) conductivities are evaluated, which are defined by the measured ionic/electronic resistance of the composite and its cell constant. The effective transport properties are accessible via DC polarization of symmetric electron-blocking and ion-blocking cells for the effective ionic ($\sigma_{\text{eff},\text{ion}}$) and the effective electronic conductivities ($\sigma_{\text{eff},\text{el}}$) respectively. A schematic of the used symmetric cells configuration is shown in the inset of Figure 3.

By varying the volume fractions of the SE and carbon, the effective ionic and electronic conductivities of the composite cathodes change. In general, the effective conductivity σ_{eff} is

related to the transport in an undisturbed volume (σ_0), i.e. the bulk conductivity, by the volume fraction of the conducting phase ϕ and the tortuosity factor τ^2 .^[112]

$$\sigma_{\text{eff}} = \frac{\phi}{\tau^2} \cdot \sigma_0. \quad (1)$$

Equation (1) quantifies the effect of a heterogeneous microstructure on the macroscopic transport, in which a high tortuosity factor lowers the corresponding transport property. When considering ionic conduction in solid-state cathode composites composed of SE, carbon and sulfur, the conducting volume fraction refers to the volume filled by the SE. In the case of electronic transport, the volume fraction of carbon is the defining parameter. Here, the Li₆PS₅Cl and carbon are assumed to be only ionically and electronically conducting, respectively. Considering the reported low electronic conductivity of lithium thiophosphate electrolytes in the order of 10⁻⁸ S·cm⁻¹, this assumption is reasonable.^[113–115]

For further quantification and comparison of the effective transport between different systems, the MacMullin number N_M [Eq. (2)], i.e. the ratio of bulk conductivity σ_0 and effective conductivity σ_{eff} , is often considered.^[79,81,82]

$$N_M = \frac{\sigma_0}{\sigma_{\text{eff}}} = \frac{\tau^2}{\phi}. \quad (2)$$

N_M reflects the ratio of the tortuosity factor τ^2 to the volume fraction of the respective conducting phase ϕ , and a high value of N_M indicates tortuous and hampered transport. In order to systematically examine the tortuosity factor, (i) the bulk conductivity σ_0 of the pristine components and (ii) the effective conductivity as a function of the volume fraction of conducting phases are quantified in the following.

- (i) *Charge transport in pristine cathode components.* For a realistic assessment of transport within the cathode composites, the partial ionic and electronic conductivities of bulk Li₆PS₅Cl and the employed carbon are measured as a baseline σ_0 for ionic and electronic transport. As cathode composites for Li–S batteries are prepared via ball-milling of the components, the pristine Li₆PS₅Cl is subjected to milling first before determination of σ_0 . While carbon additives may change the friction and impact energy in the ball mill,^[116] the milled SE is a more reasonable starting point for the assessment of the bulk conductivity than the as-prepared crystalline electrolytes. The as-synthesized crystalline Li₆PS₅Cl exhibits an ionic conductivity of 2.1 mS·cm⁻¹ (Figure S8). After the post-synthetic milling processing, the ionic conductivity is lowered to 0.58 mS·cm⁻¹. Upon ball-milling, a decreased crystallinity of Li₆PS₅Cl is observed as seen in Figure S9, in which the X-ray diffractograms show diminishing reflection intensity indicating partial amorphization. As for the pristine carbon, an electronic conductivity of 5900 mS·cm⁻¹ is obtained under standard cell conditions (Figure S10). It should be noted that, while this value will be used for $\sigma_{0,\text{el}}$ in the following analysis, it needs to be seen critically as the conductivity of the nanoporous and high-

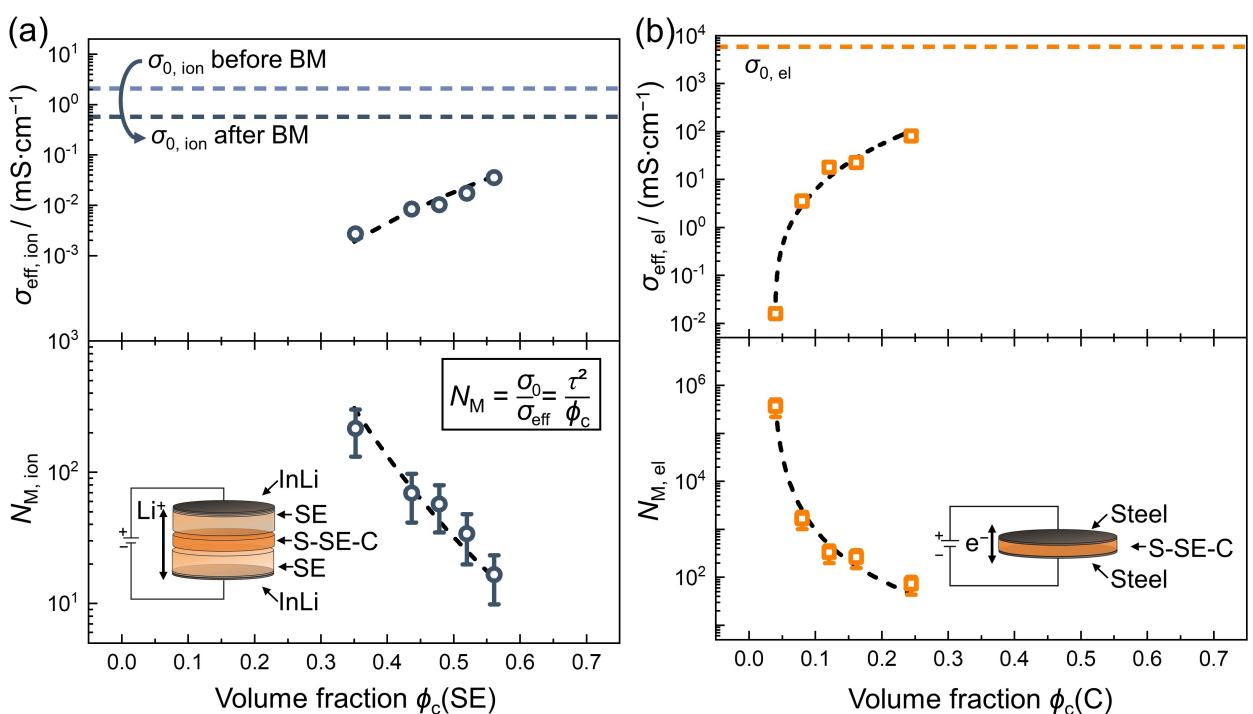


Figure 3. Effective ionic (a) and electronic conductivities (b) of as-prepared S–C–SE cathode composites deduced from DC polarization on symmetric cells (shown as insets). As electron blocking electrode, $\text{Li}_x\text{PS}_5\text{Cl}|\text{In}/\text{InLi}$ was employed. The black dashed lines represent guides to the eye. The blue and yellow dashed lines indicate the ionic and electronic conductivity of pure $\text{Li}_x\text{PS}_5\text{Cl}$ and carbon black, respectively. Due to the inferior electronic conductivity of carbon black compared to the ionic conductivity in $\text{Li}_x\text{PS}_5\text{Cl}$, cathode composites with $\phi(\text{SE}) \cdot \phi(\text{C})^{-1} > 1$ are investigated. As indicated in (a), ball-milling (BM) leads to a significant decrease in ionic conductivity of as-synthesized crystalline $\text{Li}_x\text{PS}_5\text{Cl}$. As the electronic conductivity of carbon black ($5900 \text{ mS} \cdot \text{cm}^{-1}$) exceeds the ionic conductivity of ball-milled $\text{Li}_x\text{PS}_5\text{Cl}$ ($0.58 \text{ mS} \cdot \text{cm}^{-1}$) drastically, only small amounts of carbon additives are required to achieve a sufficient effective electronic conductivity. The high MacMullin numbers N_M in the lower panels indicate impeded transport within the composite. For effective conductivities, a relative error of 20% is estimated. The error calculated for corrected volume fractions is smaller than the symbols. Errors for N_M are calculated via error propagation.

surface carbon sample will heavily depend on surface modification and packaging density.^[100,101] While the remaining porosity in a densified SE and carbon sample will decrease the experimental σ_0 compared to an ideally dense sample, here for simplicity, the MacMullin number as well as the tortuosity factor of the pure SE and carbon samples are set to unity (see below).

Two conclusions can be drawn here: Firstly, a ball-milling process drastically deteriorates the ionic conductivity of $\text{Li}_x\text{PS}_5\text{Cl}$. The reported positive effects of ball-milling on the utilization of active materials and capacity retention of Li–S cells have made ball-milling a widely used method for the preparation of solid-state cathode composites on the lab-scale.^[43,56–58] These results alone highlight the importance of tailored processing routes and the analysis of battery materials under practical conditions for a realistic performance assessment. Secondly, due to the significantly different conductivities of the pristine $\text{Li}_x\text{PS}_5\text{Cl}$ and carbon, a greater fraction of SE than that of carbon in the composite is expected to achieve sufficient ion conduction, if the ion and electron transports are hampered as a function of volume fraction in a similar manner. This will be further addressed in the following sections.

(ii) *Effective conductivities of cathode composites.* In order to elucidate the influence of conducting volume fractions on ionic and electronic transport, effective conductivities of as-

prepared S–C– $\text{Li}_x\text{PS}_5\text{Cl}$ composites shown in Figure 1 and 2 are measured. As a remaining porosity (voids) within the composite cathodes will influence the transport, the nominal volume fractions ϕ_n as shown in Figure 1 are corrected with an average porosity of 17% as listed in Table S2 (Supporting Information) on a simple fractional basis. The average porosity is calculated from experimentally found densities of densified cathode composites and the theoretical densities of the components. A more detailed discussion can be found in the Supporting Information. The resulting corrected volume fractions ϕ_c are used as a practical estimation to account for adverse effects of remaining porosity on charge transport and are employed herein to describe ionic and electronic transport. For instance, considering the best performing cell with $\phi(\text{SE}) \cdot \phi(\text{C})^{-1} = 4.0$, the nominal $\text{Li}_x\text{PS}_5\text{Cl}$ fraction of 0.58 is corrected to 0.48 to account for porosity. Correspondingly, the corrected volume fraction of carbon is 0.12 for this composite.

The effective ionic and electronic transport is quantified through DC polarization experiments and shown in Figure 3. Representative data for determining the steady-state current are shown in Figure S11. For effective conductivities, a relative measurement uncertainty of 20% is estimated based on the uncertainty of determination of the cell constant as this measurement uncertainty exceeds the one of current and

potential during DC polarization. The complete table of values is shown in the Supporting Information Table S3. With increasing volume fraction of non-conductive components, the effective conductivity drastically decreases from that of the undisturbed material as expected (Figure 3). The order of magnitude of the obtained effective conductivities is in good agreement with the previously reported values in thiophosphate-based composites, e.g. by Hakari *et al.*^[117] in 2017 for ball-milled Li₃PS₄–C composites ($\sigma_{\text{eff,ion}} = 0.06 \text{ mS} \cdot \text{cm}^{-1}$, $\sigma_{\text{eff,el}} = 15 \text{ mS} \cdot \text{cm}^{-1}$ for 30 wt.% Ketjen black in Li₃PS₄) and by Kaiser *et al.*^[90] for Li₂P₂S₈–Li₄Ti₅O₁₂–C composites ($\sigma_{\text{eff,ion}} = 0.012 \text{ mS} \cdot \text{cm}^{-1}$ for an electrolyte volume fraction of 0.4).

Figure 3 shows the MacMullin numbers N_M , representing the degree of reduction in the effective transport compared to σ_0 , which visualize the strong dependence on the conducting volume fraction. While the ionic transport in porous electrodes and separators in lithium-ion batteries with liquid electrolytes is typically described by N_M in the range of 5–20,^[73,78,79,83] the N_M values for both ion and electron transport found in this work are significantly higher, indicating tortuous and obstructed transport. Here, values of 17–220 are found for the ionic MacMullin numbers and 70–4·10⁵ for the electronic MacMullin numbers. A direct comparison of ionic and electronic transport at comparable volume fractions shows higher N_M values for ionic transport. For instance, $\phi_c(\text{SE}) = 0.35$ results in $N_{M,\text{ion}} = 220$, while for $\phi_c(\text{C}) = 0.24$, $N_{M,\text{el}} = 70$ is calculated. The here-found hampered transport, especially in the case of ionic conduction, clearly reflects highly tortuous conduction pathways in solid-state composite electrodes, which comprise a SE, an electronic conductive material, sulfur as an active material, as well as a certain fraction of porosity.

2.3. Tortuosity Analysis

The concept of tortuosity in terms of a homogenization approach allows us to describe the obstruction of charge transport in a complex microstructure. The tortuosity factor τ^2 quantifies the effect of transport that occurs along indirect and circuitous paths in a heterogeneous medium. When discussing and comparing tortuosity values, the differentiation between the geometric porosity τ and the tortuosity factor τ^2 is important. While τ is defined by the ratio of the length of a curved transport path divided by the shortest distance between start and endpoint, the tortuosity factor τ^2 is directly related to the effective transport coefficient as shown in Equation (1),^[112,118–120] and is hence employed in the following discussion. Its wide application, e.g. in the fields of fuel cells and batteries, underscores its relevance.^[82,90,118,120]

In the case of liquid electrolytes, the ion-conducting volume fraction within the cathode can be assumed to be equivalent to the porosity of the electrode materials. This is a reasonable assumption as a liquid will likely penetrate into the connected void space. Indeed, the relationships between tortuosity and pore fraction, as well as morphology of the composite and their influence on the ion transport, have been extensively studied.^[76,81,82,121,122] From the measured effective conductivities (see Figure 3) and the corrected volume fractions, we calculated the tortuosity factors (see Figure 4). Errors for tortuosity factors are derived from error propagation of the effective conductivities and standard deviation in porosities.

Within the investigated composite cathodes, the tortuosity factor of ion transport increases from 9 to 80 with the $\phi_c(\text{SE})$ being reduced from 0.56 to 0.35 (Figure 4a). Whereas ionic tortuosity factors between 1.5 and 10 are reported for oxide-based porous cathode microstructures with liquid electrolytes at

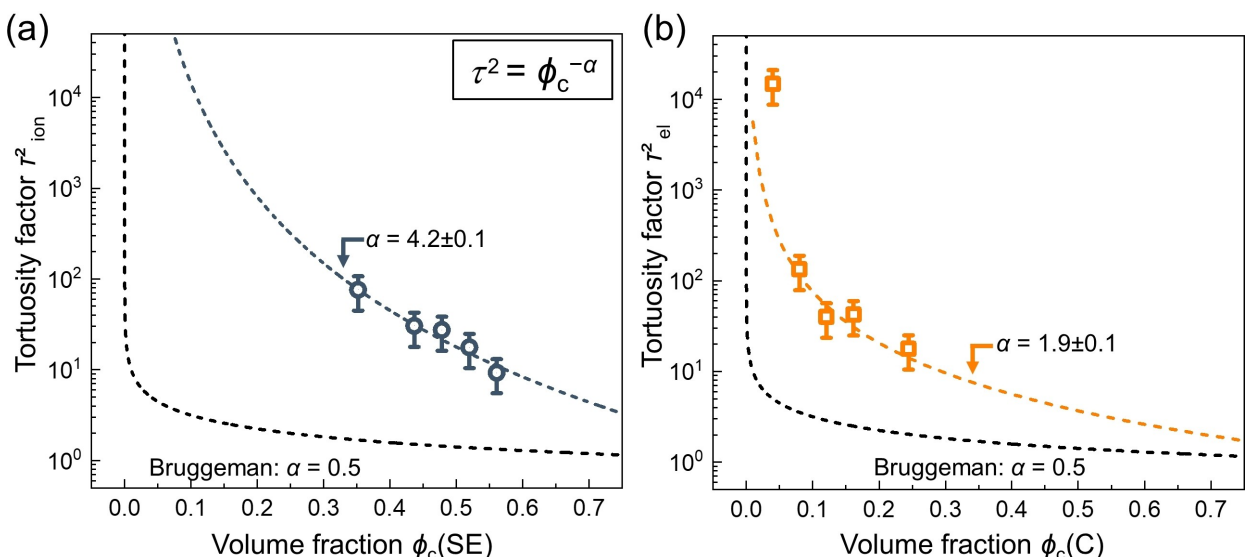


Figure 4. Estimated ionic and electronic tortuosity factors for as-synthesized S–C-Li₆PS₅Cl composites as a function of corrected volume fractions ϕ_c . Errors of tortuosity factors are derived from error propagation. At comparable volume fractions of the conducting phase, the ionic transport is described by higher tortuosity factors. For fitting, a Bruggeman-type power-law [Eq. (3)] is employed. Fitting was restricted to the effective conductivities found for cathode composites, as the inclusion of pure samples of SE and C did not lead to converging fits. The dashed black line represents an ideal Bruggeman-type function for spherical particles ($\alpha = 0.5$). Clearly, the tortuosity is underestimated by this approach and it is not applicable here.

electrolyte fractions >0.3 ,^[76,82,121,122] high ionic tortuosity factors >10 are found in this study even for $\phi_c(\text{SE})$ above 0.5. A similar trend is observed for electronic conduction. Electronic tortuosity factors of $18\text{--}1.5 \cdot 10^4$ (Figure 4b) are calculated for $\phi_c(\text{C})$ of 0.24–0.040. The significantly higher electronic tortuosity factor of 10^4 of the sample with $\phi_c(\text{C})=0.040$ may arise from a loss of percolation. The description of effective transport in heterogeneous continuous media via a simplified effective medium approach [Eq. (1)] does not account for percolation effects. When the electronic and ionic tortuosity factors are compared at similar volume fractions of conducting phases, higher ionic tortuosity factors are found within this study, highlighting that the ionic transport is more tortuous than electronic transport.

2.4. Tortuosity Factor – Conducting Volume Relation

The dependence of ionic and electronic tortuosity factors on the conducting volume fraction can be quantitatively discussed with the so-called Bruggeman relation.^[71,119,123,124] While the original model was developed to relate the tortuosity of a homogeneous suspension of insulating spherical particles in a conducting medium to the conducting volume fraction,^[125] additional fit parameters were later on introduced to adapt the equation to more complex microstructures.^[82,112,120,126] The resulting power-law [Eq. (3)]:

$$\tau^2 = \phi(x)^{-\alpha} \quad (3)$$

is employed to relate the tortuosity factor of charge transport to the volume fraction ϕ of the conducting phase x . For the case with spherical inclusions, $\alpha=0.5$ is expected.^[119] An additional prefactor is often introduced to improve fitting results in the literature,^[82,112,120,126] however, it is not employed here. As seen in Figure 4, the fit of the tortuosity factors found in this work with the Bruggeman-type power-law results in α values of 4.2 and 1.9 for ionic and electronic transport, respectively. The high α values found in this study, especially in the ionic tortuosity factor, reflect a strong dependency of the charge transport on the respective conducting volume fraction in the investigated composites. While a relatively high α for the electronic tortuosity factors may arise from a percolation issue, especially for the sample with the small $\phi_c(\text{C})=0.040$, the large α value for ionic transport is substantial. These high α values for ionic transport mean that even at high volume fractions of SE, highly tortuous pathways are expected and faster ionic conductors are needed.

Clearly, the Bruggeman relation for spherical inclusions is not valid within the investigated system. The complex cathode microstructure, *i.e.* differences in particle sizes, morphology, and residual porosity, exceeds the underlying assumptions of the Bruggeman equation. It needs to be noted that α values themselves lack real physical meaning and must be seen as empirical fitting results as a deviation from ideality. Nevertheless, these results indicate a drastically impeded charge carrier transport in the multi-component ball-milled composites and emphasize the power of this simple model to capture the

bottleneck process in composite electrolytes. The description via the straightforward power-law helps to rationally design sulfur cathode composites and fully exploit the potential of solid-state Li–S cells.

3. Discussion

The quantification of effective transport properties represents a useful approach to elucidate the limits of solid-state Li–S cells. It is important to note that effective transport can be assessed via different experimental and theoretical approaches, which may lead to varying results.^[82,86,104,112,120,122] For instance, as recently highlighted by Nguyen et al.,^[127] the effective conductivities of cathodes for lithium-ion batteries derived from steady-state current flow experiments neglect the contribution of dead-end conduction pathways to the electrochemically active surface area. However, in the case of sulfur cathodes, small particle sizes of the cathode components result in a well-dispersed microstructure. One would assume that, due to the insulating character of sulfur, ionic as well as electronic percolation is critical in order to fully utilize the theoretical capacity. Moreover, cell performance does not only depend on charge transport within the electrode and separator. Among others, interfacial stability, as well as the reversibility of active materials, will define cell life and are therefore crucial requirements for future energy storage systems. The design of optimized cathode composites and the quantification of effective conductivities is paramount and our results highlight the importance of microstructural effects on the obstruction of charge transport in solid-state sulfur-based cathode composites. Some major conclusions can be drawn:

- (i) Within this model study, mechanical mixing in a planetary ball mill is employed for composite preparation as a typically used processing technique.^[43,56,57,105] While crystalline state-of-the-art SEs show promising ionic conductivities $>1 \text{ mS} \cdot \text{cm}^{-1}$, our work shows that this value is drastically decreased by typical cathode processing and the tortuous network formed within a typical cathode. To achieve a well-dispersed and interpenetrating cathode microstructure, high energy mixing processes are required. With the ionic conductivity of $\text{Li}_6\text{PS}_5\text{Cl}$ being degraded significantly, our results highlight the importance of highly conductive, stable electrolytes and the need for an optimized processing protocol.
- (ii) The performance of all-solid-state cathodes for Li–S cells is drastically influenced by the ‘inactive’ electrode components. For complete sulfur utilization, ionic and electronic percolation by electrolyte and carbon are mandatory. Small ratios of effective ionic to effective electronic conductivity indicate the ion conduction to be limiting within the characterized system (Figure 5a), calling for high electrolyte fractions within the composites. While we focused on a model type composite with only three components in our study, additional components, *e.g.* binder, will further increase the tortuosity within an application-oriented cathode.^[112] Compared to cathodes of conventional lith-

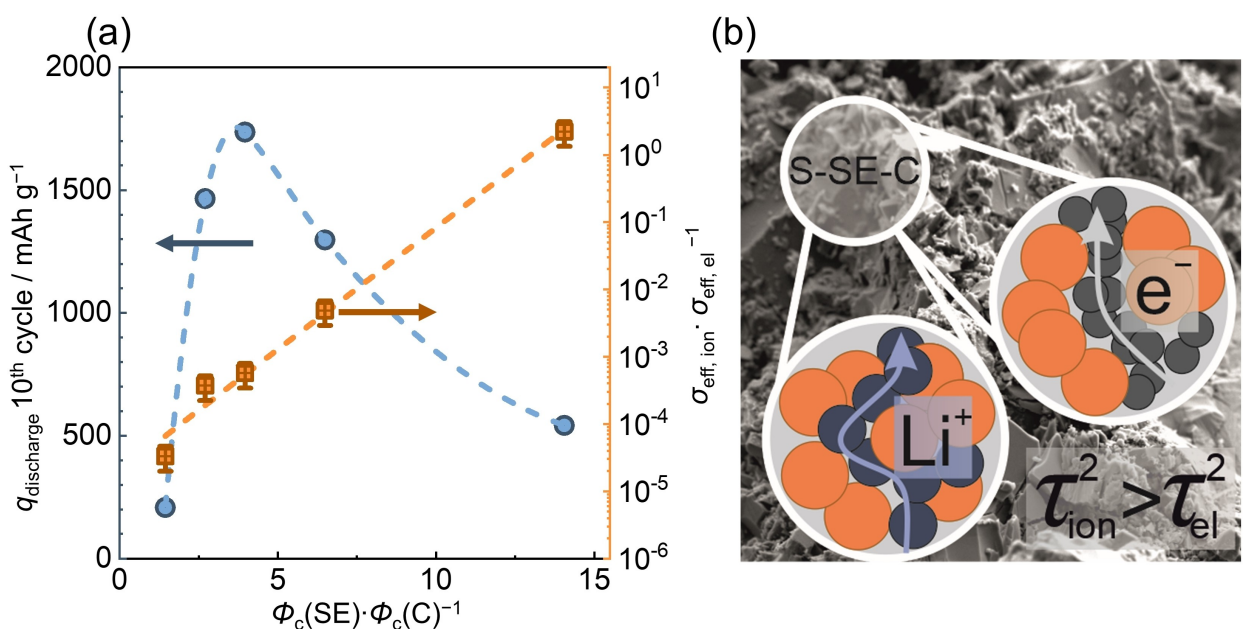


Figure 5. Specific discharge capacity of the 10th cycle (circles) and ratio of effective ionic to effective electronic conductivity (squares) as function of the volume ratio of solid electrolyte to carbon black within Li₆PS₅Cl–C–S₈ cathodes for all-solid-state Li–S cells (a). Generally, $\sigma_{\text{ion}} \cdot \sigma_{\text{el}}^{-1}$ ratios $< 10^{-2}$ highlight hampered ion transport and mark the ionic conduction as bottleneck within the studied sulfur cathodes. However, as electronic percolation is equally essential, a maximum in discharge capacity can be found for a volume ratio of around 4. The complex microstructure of an all-solid-state cathode impedes charge transport drastically, leading to low effective conductivities and high tortuosity factors. A typical solid sulfur-based cathode (b) can be described as a multi-component system with sulfur as active material (orange), carbon (dark grey) and solid electrolyte (blue). Due to intense mixing processes and residual porosity, tortuous conduction pathways for ion (blue arrow) and electron transport (grey arrow) are formed. As schematically shown, the ionic transport is assigned with higher tortuosity factors for S–C–Li₆PS₅Cl composites characterized in this study.

ium-ion batteries with liquid electrolytes, the convoluted and heterogeneous microstructure of solid-state sulfur cathodes obstructs charge transport even more (Figure 5b). In the case of all-solid systems, especially the porosity plays an important role and needs to be discussed. While pores are filled effectively by liquid electrolytes, they impede the transport when SEs are employed. The related constriction of conduction pathways decreases the effective conductivities.

(iii) In principle, the effective ionic conductivity can be increased via the reduction of tortuosity by a tailored electrode architecture and/or the implementation of highly conductive electrolytes that keep their high conductivity even after processing.^[7,55,90,128–133] The implementation of a low-tortuous carbon scaffold as well as mixtures of different carbon species, e.g. one- or two-dimensional carbons, may help to reduce the volume fraction of carbon required for electronic percolation.^[134] However, as both sulfur and carbon are employed in small particle sizes, the design of the SE morphology, particle sizes as well as size distribution stands out as an optimization strategy for solid-state cathodes.^[135] However, due to the sensitivity of the employed crystalline thiophosphate, a careful approach is needed here to retain its high ionic conductivity. Here, temperature-assisted ball-milling under mild conditions or solution-based synthesis in combination with short annealing may represent promising strategies.^[58,136,137] Furthermore, strategies to reduce the remaining porosity, e.g. by the design of particle sizes, tailored densification protocols

and filling with liquid/polymer electrolytes, can be expected to decrease the MacMullin number and tortuosity of all-solid-state electrodes effectively.^[71,130]

(iv) With the presented study highlighting the tortuous transport within as-prepared composites, it is important to emphasize that charge transport was quantified for pristine cathodes only. Cycling and side reactions may change the effective conductivities. The reactivity of thiophosphate electrolytes, as well as chemical and morphological changes due to the cell reaction during cycling, will alter the charge transport within a cathode as the cell is being cycled.^[104] As only the properties of the as-prepared composites are investigated within this study, the evaluation of changes in transport properties during battery operation is needed for a future, realistic assessment of all-solid-state Li–S cells. Additionally, variations in the volume fraction of sulfur within the cathode (which was kept constant in this study) will lead to alterations in ionic and electronic transport. Hence, aiming for a performance optimization, the occurring charge transport needs to be quantified for the individual system.

4. Conclusions

In order to put competitive all-solid-state Li–S cells into practice, the mass loading of active materials compared to lab-scale studies needs to be maximized whereas inactive cell components are reduced. As a first step, characterizing the

limiting charge transport processes within a solid-state cathode composite helps to understand and optimize cell performance. In this study, the ionic conduction is identified as the bottleneck in sulfur-based solid-state cathodes at a practical sulfur loading of $3.8 \text{ mg} \cdot \text{cm}^{-2}$. While intense mixing processes are required to fully utilize the high theoretical capacity, the high ionic conductivity of crystalline $\text{Li}_6\text{PS}_5\text{Cl}$ is drastically reduced by intense processing contributing to low effective ionic conductivities of cathode composites. As this highlights the importance of the evaluation of battery materials under practical conditions, the optimization of cathode processing appears necessary for crystalline $\text{Li}_6\text{PS}_5\text{Cl}$.

The complex cathode microstructure impedes charge transport and leads to tortuous conduction pathways. For the investigated systems, the Bruggeman equation for spherical inclusions is not valid. While this model is often employed in porous electrodes for batteries with liquid electrolytes, differences in particle sizes and morphology as well as residual porosity in an all-solid system further deteriorate charge transport and lead to an underestimation of tortuosity values for all-solid-state systems by the classical empirical equation.

In order to increase the effective conductivities of electrodes and to maximize the areal capacity, the implementation of highly conductive electrolytes as well as tailored architectures represent possible optimization strategies. However, regarding the herein investigated model system, our results especially emphasize the importance of further research on solid electrolytes. Here, mechanical stability, good processability and high ionic conductivity are required. For solid-state Li–S cells with high energy density, ionic conductivities exceeding those of the employed thiophosphate seem necessary, as high electrolyte fractions composite are necessary to address the full theoretical capacity based on the state-of-the-art solid electrolytes. With our results underscoring the importance of a well-designed cathode microstructure and a tailored processing protocol, further research is required to fully address the remarkable theoretical performance of solid-state Li–S cells.

Acknowledgements

The research was supported by the Federal Ministry of Education and Research (BMBF) within the project LISZUBA under grant number 03XP0115A. The authors thank Dominik Steckermeier and Prof. Dr. Arno Kwade (Technische Universität Braunschweig) for the preparation of sulfur–carbon composites. Open access funding enabled and organized by Projekt DEAL.

Conflict of Interest

The authors declare no conflict of interest.

Keywords: charge transport · composite cathode · conversion electrode · lithium-sulfur solid-state batteries · tortuosity factor

- [1] A. Manthiram, Y. Fu, S. H. Chung, C. Zu, Y. S. Su, *Chem. Rev.* **2014**, *114*, 11751–11787.
- [2] M. Wild, L. O'Neill, T. Zhang, R. Purkayastha, G. Minton, M. Marinescu, G. J. Offer, *Energy Environ. Sci.* **2015**, *8*, 3477–3494.
- [3] Y. X. Yin, S. Xin, Y. G. Guo, L. J. Wan, *Angew. Chem. Int. Ed.* **2013**, *52*, 13186–13200; *Angew. Chem.* **2013**, *125*, 13426–13441.
- [4] P. G. Bruce, S. A. Freunberger, L. J. Hardwick, J. M. Tarascon, *Nat. Mater.* **2012**, *11*, 19–29.
- [5] M. Rana, S. A. Ahad, M. Li, B. Luo, L. Wang, I. Gentle, R. Knibbe, *Energy Storage Mater.* **2019**, *18*, 289–310.
- [6] M. Hagen, D. Hanselmann, K. Ahlbrecht, R. Maça, D. Gerber, J. Tübke, *Adv. Energy Mater.* **2015**, *5*, 1401986.
- [7] T. Li, X. Bai, U. Gulzar, Y. J. Bai, C. Capiglia, W. Deng, X. Zhou, Z. Liu, Z. Feng, R. Proietti Zaccaria, *Adv. Funct. Mater.* **2019**, *29*, 1901730.
- [8] Z. Lin, C. Liang, *J. Mater. Chem. A* **2015**, *3*, 936–958.
- [9] A. F. Hofmann, D. N. Fronczek, W. G. Bessler, *J. Power Sources* **2014**, *259*, 300–310.
- [10] Y. Diao, K. Xie, S. Xiong, X. Hong, *J. Power Sources* **2013**, *235*, 181–186.
- [11] M. R. Busche, P. Adelhelm, H. Sommer, H. Schneider, K. Leitner, J. Janek, *J. Power Sources* **2014**, *259*, 289–299.
- [12] B. Liu, R. Fang, D. Xie, W. Zhang, H. Huang, Y. Xia, X. Wang, X. Xia, J. Tu, *Energy Environ. Mater.* **2018**, *1*, 196–208.
- [13] M. Agostini, Y. Aihara, T. Yamada, B. Scrosati, J. Hassoun, *Solid State Ionics* **2013**, *244*, 48–51.
- [14] H. Nagata, Y. Chikusa, *Energy Technol.* **2016**, *4*, 484–489.
- [15] U. Ulissi, S. Ito, S. M. Hosseini, A. Varzi, Y. Aihara, S. Passerini, *Adv. Energy Mater.* **2018**, *8*, 1801462.
- [16] D. Lei, K. Shi, H. Ye, Z. Wan, Y. Wang, L. Shen, B. Li, Q. H. Yang, F. Kang, Y. B. He, *Adv. Funct. Mater.* **2018**, *28*, 1707570.
- [17] J. Janek, W. G. Zeier, *Nat. Energy* **2016**, *1*, 16141.
- [18] Z. Zhang, Y. Shao, B. Lotsch, Y. S. Hu, H. Li, J. Janek, L. F. Nazar, C. W. Nan, J. Maier, M. Armand, L. Chen, *Energy Environ. Sci.* **2018**, *11*, 1945–1976.
- [19] T. Yamada, S. Ito, R. Omoda, T. Watanabe, Y. Aihara, M. Agostini, U. Ulissi, J. Hassoun, B. Scrosati, *J. Electrochem. Soc.* **2015**, *162*, A646–A651.
- [20] S. Ohno, A. Banik, G. F. Dewald, M. A. Kraft, T. Krauskopf, N. Minafra, P. Till, M. Weiss, W. G. Zeier, *Prog. Energy* **2020**, *2*, 022001.
- [21] P. Bonnick, K. Niitani, M. Nose, K. Suto, T. S. Arthur, J. Muldoon, *J. Mater. Chem. A* **2019**, *7*, 24173–24179.
- [22] M. Nagao, A. Hayashi, M. Tatsumisago, *J. Mater. Chem.* **2012**, *22*, 10015–10020.
- [23] Y. Aihara, S. Ito, R. Omoda, T. Yamada, S. Fujiki, T. Watanabe, Y. Park, S. Doo, *Front. Energy Res.* **2016**, *4*, 1–8.
- [24] T. Hakari, A. Hayashi, M. Tatsumisago, *Chem. Lett.* **2015**, *44*, 1664–1666.
- [25] M. A. Kraft, S. Ohno, T. Zinkevich, R. Koerver, S. P. Culver, T. Fuchs, A. Senyshyn, S. Indris, B. J. Morgan, W. G. Zeier, *J. Am. Chem. Soc.* **2018**, *140*, 16330–16339.
- [26] N. Kamaya, K. Homma, Y. Yamakawa, M. Hirayama, R. Kanno, M. Yonemura, T. Kamiyama, Y. Kato, S. Hama, K. Kawamoto, A. Mitsui, *Nat. Mater.* **2011**, *10*, 682–686.
- [27] A. Sakuda, A. Hayashi, M. Tatsumisago, *Sci. Rep.* **2013**, *3*, 2261.
- [28] S. Ohno, B. Helm, T. Fuchs, G. Dewald, M. A. Kraft, S. P. Culver, A. Senyshyn, W. G. Zeier, *Chem. Mater.* **2019**, *31*, 4936–4944.
- [29] Y. Kato, S. Hori, T. Saito, K. Suzuki, M. Hirayama, R. Kanno, M. Yonemura, H. Iba, R. Kanno, *Nat. Energy* **2016**, *1*, 16030.
- [30] Y. Zhu, X. He, Y. Mo, *ACS Appl. Mater. Interfaces* **2015**, *7*, 23685–23693.
- [31] W. Zhang, F. H. Richter, S. P. Culver, T. Leichtweiss, J. G. Lozano, C. Dietrich, P. G. Bruce, W. G. Zeier, J. Janek, *ACS Appl. Mater. Interfaces* **2018**, *10*, 22226–22236.
- [32] R. Koerver, F. Walther, I. Aygün, J. Sann, C. Dietrich, W. G. Zeier, J. Janek, *J. Mater. Chem. A* **2017**, *5*, 22750–22760.
- [33] F. Walther, R. Koerver, T. Fuchs, S. Ohno, J. Sann, M. Rohnke, W. G. Zeier, J. Janek, *Chem. Mater.* **2019**, *31*, 3745–3755.
- [34] Y. S. Jung, D. Y. Oh, Y. J. Nam, K. H. Park, *Isr. J. Chem.* **2015**, *55*, 472–485.
- [35] M. Hagen, P. Fanz, J. Tübke, *J. Power Sources* **2014**, *264*, 30–34.
- [36] J. Brückner, S. Thieme, H. T. Grossmann, S. Dörfler, H. Althues, S. Kaskel, *J. Power Sources* **2014**, *268*, 82–87.
- [37] Q. Pang, A. Shyamsunder, B. Narayanan, C. Y. Kwok, L. A. Curtiss, L. F. Nazar, *Nat. Energy* **2018**, *3*, 783–791.
- [38] G. He, X. Ji, L. Nazar, *Energy Environ. Sci.* **2011**, *4*, 2878–2883.
- [39] G. He, S. Evers, X. Liang, M. Cuisinier, A. Garsuch, L. F. Nazar, *ACS Nano* **2013**, *7*, 10920–10930.

- [40] Q. Pang, X. Liang, C. Y. Kwok, L. F. Nazar, *Nat. Energy* **2016**, *1*, 16132.
- [41] X. Ji, K. T. Lee, L. F. Nazar, *Nat. Mater.* **2009**, *8*, 500–506.
- [42] S. Thieme, J. Brückner, A. Meier, I. Bauer, K. Gruber, J. Kaspar, A. Helmer, H. Althues, M. Schmuck, S. Kaskel, *J. Mater. Chem. A* **2015**, *3*, 3808–3820.
- [43] S. Ohno, R. Koerver, G. Dewald, C. Rosenbach, P. Titscher, D. Steckermeier, A. Kwade, J. Janek, W. G. Zeier, *Chem. Mater.* **2019**, *31*, 2930–2940.
- [44] X. Yang, J. Luo, X. Sun, *Chem. Soc. Rev.* **2020**, *49*, 2140–2195.
- [45] W. Zhang, T. Leichtweiß, S. P. Culver, R. Koerver, D. Das, D. A. Weber, W. G. Zeier, J. Janek, *ACS Appl. Mater. Interfaces* **2017**, *9*, 35888–35896.
- [46] G. F. Dewald, S. Ohno, M. A. Kraft, R. Koerver, P. Till, N. M. Vargas-Barbosa, J. Janek, W. G. Zeier, *Chem. Mater.* **2019**, *31*, 8328–8337.
- [47] T. Swamy, X. Chen, Y.-M. Chiang, *Chem. Mater.* **2019**, *31*, 707–713.
- [48] F. Walther, S. Randau, Y. Schneider, J. Sann, M. Rohnke, F. H. Richter, W. G. Zeier, J. Janek, *Chem. Mater.* **2020**, *32*, 6123–6136.
- [49] W. Zhang, D. Schröder, T. Arlt, I. Manke, R. Koerver, R. Pinedo, D. A. Weber, J. Sann, W. G. Zeier, J. Janek, *J. Mater. Chem. A* **2017**, *5*, 9929–9936.
- [50] R. Koerver, I. Aygün, T. Leichtweiß, C. Dietrich, W. Zhang, J. O. Binder, P. Hartmann, W. G. Zeier, J. Janek, *Chem. Mater.* **2017**, *29*, 5574–5582.
- [51] C. Yu, S. Ganapathy, E. R. H. V. Eck, H. Wang, S. Basak, Z. Li, M. Wagemaker, *Nat. Commun.* **2017**, *8*, 1086.
- [52] J. Tippens, J. C. Miers, A. Afshar, J. A. Lewis, F. J. Q. Cortes, H. Qiao, T. S. Marchese, C. V. Di Leo, C. Saldana, M. T. McDowell, *ACS Energy Lett.* **2019**, *4*, 1475–1483.
- [53] K. Suzuki, N. Mashimo, Y. Ikeda, T. Yokoi, M. Hirayama, R. Kanno, *ACS Appl. Energy Mater.* **2018**, *1*, 2373–2377.
- [54] K. Suzuki, D. Kato, K. Hara, T. A. Yano, M. Hirayama, M. Hara, R. Kanno, *Electrochemistry* **2018**, *86*, 1–5.
- [55] M. Li, R. Carter, A. Douglas, L. Oakes, C. L. Pint, *ACS Nano* **2017**, *11*, 4877–4884.
- [56] M. Chen, S. Adams, *J. Solid State Electrochem.* **2015**, *19*, 697–702.
- [57] X. Yao, N. Huang, F. Han, Q. Zhang, H. Wan, J. P. Mwizerwa, C. Wang, X. Xu, *Adv. Energy Mater.* **2017**, *7*, 1602923.
- [58] K. Suzuki, D. Kato, K. Hara, T. aki Yano, M. Hirayama, M. Hara, R. Kanno, *Electrochim. Acta* **2017**, *258*, 110–115.
- [59] A. Sakuda, Y. Sato, A. Hayashi, M. Tatsumisago, *Energy Technol.* **2019**, *7*, 1900077.
- [60] T. Kobayashi, Y. Imade, D. Shishihara, K. Homma, M. Nagao, R. Watanabe, T. Yokoi, A. Yamada, R. Kanno, T. Tatsumi, *J. Power Sources* **2008**, *182*, 621–625.
- [61] S. Randau, D. A. Weber, O. Kötz, R. Koerver, P. Braun, A. Weber, E. Ivers-Tiffée, T. Adermann, J. Kulisch, W. G. Zeier, F. H. Richter, J. Janek, *Nat. Energy* **2020**, *5*, 259–270.
- [62] D. Schmidt, M. Kamla, V. Knoblauch, *J. Energy Storage* **2018**, *17*, 213–223.
- [63] C. Huang, P. S. Grant, *J. Mater. Chem. A* **2018**, *6*, 14689–14699.
- [64] S. H. Lee, S. Lee, B. S. Jin, H. S. Kim, *Sci. Rep.* **2019**, *9*, 8901.
- [65] X. Lu, A. Bertei, D. P. Finegan, C. Tan, S. R. Daemi, J. S. Weaving, K. B. O'Regan, T. M. M. Heenan, G. Hinds, E. Kendrick, D. J. L. Brett, P. R. Shearing, *Nat. Commun.* **2020**, *11*, 2079.
- [66] K. Kuchler, B. Prifling, D. Schmidt, H. Markötter, I. Manke, T. Bernthal, V. Knoblauch, V. Schmidt, *J. Microsc.* **2018**, *272*, 96–110.
- [67] Y. Kato, S. Shiotani, K. Morita, K. Suzuki, M. Hirayama, R. Kanno, *J. Phys. Chem. Lett.* **2018**, *9*, 607–613.
- [68] F. Strauss, T. Bartsch, L. de Biasi, A. Y. Kim, J. Janek, P. Hartmann, T. Brezesinski, *ACS Energy Lett.* **2018**, *3*, 992–996.
- [69] S. Choi, M. Jeon, J. Ahn, W. D. Jung, S. M. Choi, J. S. Kim, J. Lim, Y. J. Jang, H. G. Jung, J. H. Lee, B. I. Sang, H. Kim, *ACS Appl. Mater. Interfaces* **2018**, *10*, 23740–23747.
- [70] A. Neumann, S. Randau, K. Becker-Steinberger, T. Danner, S. Hein, Z. Ning, J. Marrow, F. H. Richter, J. Janek, A. Latz, *ACS Appl. Mater. Interfaces* **2020**, *12*, 9277–9291.
- [71] D. Hlushkou, A. E. Reising, N. Kaiser, S. Spannenberger, S. Schlabach, Y. Kato, B. Roling, U. Tallarek, *J. Power Sources* **2018**, *396*, 363–370.
- [72] A. Bielefeld, D. A. Weber, J. Janek, *J. Phys. Chem. C* **2019**, *123*, 1626–1634.
- [73] J. Park, D. Kim, W. A. Appiah, J. Song, K. T. Bae, K. T. Lee, J. Oh, J. Y. Kim, Y. G. Lee, M. H. Ryou, Y. M. Lee, *Energy Storage Mater.* **2019**, *19*, 124–129.
- [74] R. García-García, R. E. García, *J. Power Sources* **2016**, *309*, 11–19.
- [75] G. J. Nelson, B. N. Cassenti, A. A. Peracchio, W. K. S. Chiu, *J. Electrochem. Soc.* **2012**, *159*, A598–A603.
- [76] M. Ebner, D. W. Chung, R. E. García, V. Wood, *Adv. Energy Mater.* **2014**, *4*, 1301278.
- [77] D. Djian, F. Alloin, S. Martinet, H. Lignier, J. Y. Sanchez, *J. Power Sources* **2007**, *172*, 416–421.
- [78] R. Zahn, M. F. Lagadec, V. Wood, *ACS Energy Lett.* **2017**, *2*, 2452–2453.
- [79] K. K. Patel, J. M. Paulsen, J. Desilvestro, *J. Power Sources* **2003**, *122*, 144–152.
- [80] P. Pietsch, D. Westhoff, J. Feinauer, J. Eller, F. Marone, M. Stampanoni, V. Schmidt, V. Wood, *Nat. Commun.* **2016**, *7*, 12909.
- [81] I. V. Thorat, D. E. Stephenson, N. A. Zacharias, K. Zaghib, J. N. Harb, D. R. Wheeler, *J. Power Sources* **2009**, *188*, 592–600.
- [82] J. Landesfeind, J. Hattendorff, A. Ehrl, W. A. Wall, H. A. Gasteiger, *J. Electrochem. Soc.* **2016**, *163*, A1373–A1387.
- [83] T. DuBeshter, P. K. Sinha, A. Sakars, G. W. Fly, J. Jorne, *J. Electrochem. Soc.* **2014**, *161*, A599–A605.
- [84] T. Hutzenlaub, A. Asthana, J. Becker, D. R. Wheeler, R. Zengerle, S. Thiele, *Electrochem. Commun.* **2013**, *27*, 77–80.
- [85] B. T. Habte, F. Jiang, *Microporous Mesoporous Mater.* **2018**, *268*, 69–76.
- [86] Z. Siroma, T. Sato, T. Takeuchi, R. Nagai, A. Ota, T. Ioroi, *J. Power Sources* **2016**, *316*, 215–223.
- [87] J. Auvergniot, A. Cassel, D. Foix, V. Viallet, V. Seznec, R. Dedryvère, *Solid State Ionics* **2017**, *300*, 78–85.
- [88] H. Jiang, Y. Han, H. Wang, Q. Guo, Y. Zhu, W. Xie, C. Zheng, K. Xie, *Ionics* **2020**, *26*, 2335–2342.
- [89] D. H. S. Tan, A. Banerjee, Z. Chen, Y. S. Meng, *Nat. Nanotechnol.* **2020**, *15*, 170–180.
- [90] N. Kaiser, S. Spannenberger, M. Schmitt, M. Cronau, Y. Kato, B. Roling, *J. Power Sources* **2018**, *396*, 175–181.
- [91] T. Asano, S. Yubuchi, A. Sakuda, A. Hayashi, M. Tatsumisago, *J. Electrochem. Soc.* **2017**, *164*, A3960–A3963.
- [92] S. Wenzel, S. J. Sedlmaier, C. Dietrich, W. G. Zeier, J. Janek, *Solid State Ionics* **2018**, *318*, 102–112.
- [93] A. L. Santhosa, L. Medenbach, J. R. Buchheim, P. Adelhelm, *Batteries Supercaps* **2019**, *2*, 524–529.
- [94] S. Boulineau, J. M. Tarascon, J. B. Leriche, V. Viallet, *Solid State Ionics* **2013**, *242*, 45–48.
- [95] W. D. Richards, L. J. Miara, Y. Wang, J. C. Kim, G. Ceder, *Chem. Mater.* **2016**, *28*, 266–273.
- [96] J. Auvergniot, A. Cassel, J. B. Ledeuil, V. Viallet, V. Seznec, R. Dedryvère, *Chem. Mater.* **2017**, *29*, 3883–3890.
- [97] S. Wang, X. Xu, X. Zhang, C. Xin, B. Xu, L. Li, Y. H. Lin, Y. Shen, B. Li, C. W. Nan, *J. Mater. Chem. A* **2019**, *7*, 18612–18618.
- [98] N. C. Rosero-Navarro, A. Miura, K. Tadanaga, *J. Power Sources* **2018**, *396*, 33–40.
- [99] Y. Kuang, C. Chen, D. Kirsch, L. Hu, *Adv. Energy Mater.* **2019**, *9*, 1901457.
- [100] A. Celzard, J. F. Maréché, F. Payot, G. Furdin, *Carbon* **2002**, *40*, 2801–2815.
- [101] D. Pantea, H. Darmstadt, S. Kaliaguine, C. Roy, *Appl. Surf. Sci.* **2003**, *217*, 181–193.
- [102] J. F. Shackelford, Y.-H. Han, S. Kim, S.-H. Kwon, *CRC Materials Science and Engineering Handbook*, CRC Press, Boca Raton **2015**.
- [103] M. A. Kraft, S. P. Culver, M. Calderon, F. Böcher, T. Krauskopf, A. Senyshyn, C. Dietrich, A. Zevalkink, J. Janek, W. G. Zeier, *J. Am. Chem. Soc.* **2017**, *139*, 10909–10918.
- [104] S. Ohno, C. Rosenbach, G. F. Dewald, J. Janek, W. G. Zeier, *submitted 2020*, A comprehensive study on thiophosphate-based composite cathodes toward solid-state lithium-sulfur batteries: stability reversibility, and charge carrier transport. Department for Applied Chemistry, Kyushu University, Fukuoka, Japan.
- [105] F. Han, J. Yue, X. Fan, T. Gao, C. Luo, Z. Ma, L. Suo, C. Wang, *Nano Lett.* **2016**, *16*, 4521–4527.
- [106] T. K. Schwietert, V. A. Arszelewska, C. Wang, C. Yu, A. Vasileiadis, N. J. J. de Klerk, J. Hageman, T. Hupfer, I. Kerkamm, Y. Xu, E. van der Maas, E. M. Kelder, S. Ganapathy, M. Wagemaker, *Nat. Mater.* **2020**, *19*, 428–435.
- [107] D. H. S. Tan, E. A. Wu, H. Nguyen, Z. Chen, M. A. T. Marple, J. M. Doux, X. Wang, H. Yang, A. Banerjee, Y. S. Meng, *ACS Energy Lett.* **2019**, *4*, 2418–2427.
- [108] H. J. Peng, J. Q. Huang, X. B. Cheng, Q. Zhang, *Adv. Energy Mater.* **2017**, *7*, 170260.
- [109] X. Qi, B. Blizanac, A. Dupasquier, M. Oljaca, J. Li, M. Winter, *Carbon* **2013**, *64*, 334–340.
- [110] H. Zheng, R. Yang, G. Liu, X. Song, V. S. Battaglia, *J. Phys. Chem. C* **2012**, *116*, 4875–4882.

- [111] F. Strauss, D. Stepien, J. Maibach, L. Pfaffmann, S. Indris, P. Hartmann, T. Brezesinski, *RSC Adv.* **2019**, *10*, 1114–1119.
- [112] A. Bielefeld, D. A. Weber, J. Janek, *ACS Appl. Mater. Interfaces* **2020**, *12*, 12821–12833.
- [113] B. R. Shin, Y. J. Nam, D. Y. Oh, D. H. Kim, J. W. Kim, Y. S. Jung, *Electrochim. Acta* **2014**, *146*, 395–402.
- [114] K. Minami, F. Mizuno, A. Hayashi, M. Tatsumisago, *Solid State Ionics* **2007**, *178*, 837–841.
- [115] S. Boulaineau, M. Courty, J. M. Tarascon, V. Viallet, *Solid State Ionics* **2012**, *221*, 1–5.
- [116] C. F. Burmeister, A. Kwade, *Chem. Soc. Rev.* **2013**, *42*, 7660–7667.
- [117] T. Hakari, Y. Sato, S. Yoshimi, A. Hayashi, M. Tatsumisago, *J. Electrochem. Soc.* **2017**, *164*, A2804–A2811.
- [118] L. Holzer, D. Wiedenmann, B. Münch, L. Keller, M. Prestat, P. Gasser, I. Robertson, B. Grobety, *J. Mater. Sci.* **2013**, *48*, 2934–2952.
- [119] B. Tjaden, S. J. Cooper, D. J. Brett, D. Kramer, P. R. Shearing, *Curr. Opin. Chem. Eng.* **2016**, *12*, 44–51.
- [120] B. Tjaden, D. J. L. Brett, P. R. Shearing, *Int. Mater. Rev.* **2018**, *63*, 47–67.
- [121] C. L. Cobb, C.-J. Bae, *ECS Trans.* **2014**, *58*, 13–24.
- [122] F. L. E. Usseglio-Viretta, A. Colclasure, A. N. Mistry, K. P. Y. Claver, F. Pouraghajan, D. P. Finegan, T. M. M. Heenan, D. Abraham, P. P. Mukherjee, D. Wheeler, P. Shearing, S. J. Cooper, K. Smith, *J. Electrochem. Soc.* **2018**, *165*, A3403–A3426.
- [123] D. W. Chung, M. Ebner, D. R. Ely, V. Wood, R. Edwin García, *Modell. Simul. Mater. Sci. Eng.* **2013**, *21*, 074009.
- [124] L. Zhang, X. Zhan, Y. T. Cheng, M. Shirpour, *J. Phys. Chem. Lett.* **2017**, *8*, 5385–5389.
- [125] D. A. G. Bruggeman, *Ann. Phys.* **1935**, *416*, 636–664.
- [126] L. Froboese, J. F. van der Sichel, T. Loellhoeffel, L. Helmers, A. Kwade, *J. Electrochem. Soc.* **2019**, *166*, A318–A328.
- [127] T.-T. Nguyen, A. Demortière, B. Fleutot, B. Delobel, C. Delacourt, S. J. Cooper, *npj Comput. Mater.* **2020**, *6*, 123.
- [128] C. Chen, Y. Zhang, Y. Li, Y. Kuang, J. Song, W. Luo, Y. Wang, Y. Yao, G. Pastel, J. Xie, L. Hu, *Adv. Energy Mater.* **2017**, *7*, 1700595.
- [129] Y. Li, K. K. Fu, C. Chen, W. Luo, T. Gao, Y. Dai, G. Pastel, Y. Wang, B. Liu, J. Song, Y. Chen, C. Yang, L. Hu, *ACS Nano* **2017**, *11*, 4801–4807.
- [130] C. J. Bae, C. K. Erdonmez, J. W. Halloran, Y. M. Chiang, *Adv. Mater.* **2013**, *25*, 1254–1258.
- [131] Y. Hu, W. Chen, T. Lei, Y. Jiao, J. Huang, A. Hu, C. Gong, C. Yan, X. Wang, J. Xiong, *Adv. Energy Mater.* **2020**, 2000082.
- [132] Z. Jiao, L. Chen, J. Si, C. Xu, Y. Jiang, Y. Zhu, Y. Yang, B. Zhao, *J. Power Sources* **2017**, *353*, 167–175.
- [133] L. Peng, Y. Zhu, D. Chen, R. S. Ruoff, G. Yu, *Adv. Energy Mater.* **2016**, *6*, 1600025.
- [134] H. Kim, J. T. Lee, A. Magasinski, K. Zhao, Y. Liu, G. Yushin, *Adv. Energy Mater.* **2015**, *5*, 1501306.
- [135] T. Shi, Q. Tu, Y. Tian, Y. Xiao, L. J. Miara, O. Kononova, G. Ceder, *Adv. Energy Mater.* **2020**, *10*, 1902881.
- [136] M. Ghidiu, J. Ruhl, S. P. Culver, W. G. Zeier, *J. Mater. Chem. A* **2019**, *7*, 17735–17753.
- [137] K. H. Park, Q. Bai, D. H. Kim, D. Y. Oh, Y. Zhu, Y. Mo, Y. S. Jung, *Adv. Energy Mater.* **2018**, *8*, 1800035.

Manuscript received: August 17, 2020

Revised manuscript received: September 10, 2020

Accepted manuscript online: September 14, 2020

Version of record online: October 7, 2020